Atmospheric Research 218 (2019) 78–89

Contents lists available at ScienceDirect

Atmospheric Research

journal homepage: www.elsevier.com/locate/atmosres

Seasonal analysis of the atmosphere during five years by using microwave radiometry over a mid-latitude site

Andrés Esteban Bedoya-Velásquez[a,b,c,*], Francisco Navas-Guzmán[d], Gregori de Arruda Moreira[a,b,f], Roberto Román[a,b,e], Alberto Cazorla[a,b], Pablo Ortiz-Amezcua[a,b], José Antonio Benavent-Oltra[a,b], Lucas Alados-Arboledas[a,b], Francisco José Olmo-Reyes[a,b], Inmaculada Foyo-Moreno[a,b], Elena Montilla-Rosero[g], Carlos D. Hoyos[h], Juan Luis Guerrero-Rascado[a,b]

[a] Andalusian Institute for Earth System Research (IISTA-CEAMA), University of Granada, Autonomous Government of Andalusia, 18006 Granada, Spain
[b] Department of Applied Physics, University of Granada, Granada, Spain
[c] Facultad de Ciencias, Departamento de Física, Universidad Nacional de Colombia, Medellín, Colombia
[d] Federal Office of Meteorology and Climatology MeteoSwiss, Payerne, Switzerland
[e] Atmospheric Optics Group (GOA-UVa), Valladolid University, Valladolid, Spain
[f] Institute of Research and Nuclear Energy, IPEN, São Paulo, Brazil
[g] Physical Sciences Department, School of Science, EAFIT University, Medellín, Colombia
[h] Facultad de Minas, Departamento de Geociencias y Medio Ambiente, Universidad Nacional de Colombia, Medellín, Colombia

ARTICLE INFO

Keywords:
Microwave radiometry
Passive remote sensing
Thermodynamic characterization of atmosphere
Atmospheric boundary layer

ABSTRACT

This work focuses on the analysis of the seasonal cycle of temperature and relative humidity (RH) profiles and integrated water vapor (IWV) obtained from microwave radiometer (MWR) measurements over the mid-latitude city of Granada, southern Spain. For completeness the study, the maximum atmospheric boundary layer height ($ABLH^{max}$) is also included. To this end, we have firstly characterized the HATPRO-RPG MWR errors using 55 co-located radiosondes (RS) by means of the mean-bias ($\overline{bias}$) profile and the standard deviation (SD_{bias}) profile classified under all-weather conditions and cloud-free conditions.

This characterization pointed out that temperature from HATPRO-MWR presents a very low $\overline{bias}$ respects RS mostly below 2.0 km agl, ranging from positive to negative values under all-weather conditions (from 1.7 to −0.4 K with SD_{bias} up to 3.0 K). Under cloud-free conditions, the bias was very similar to that found under all-weather conditions (1.8 to −0.4 K) but with smaller SD_{bias} (up to 1.1 K). The same behavior is also seen in this lower part (ground to 2.0 km agl) for RH. Under all-weather conditions, the mean RH bias ranged from 3.0 to −4.0% with SD_{bias} between 10 and 16.3% while under cloud-free conditions the bias ranged from 2.0 to −0.4% with SD_{bias} from 0.5 to 13.3%. Above 2.0 km agl, the SD_{bias} error increases considerably up to 4 km agl (up to −20%), and then decreases slightly above 7.0 km agl (up to −5%). In addition, IWV values from MWR were also compared with the values obtained from the integration of RS profiles, showing a better linear fit under cloud-free conditions ($R^2 = 0.96$) than under all-weather conditions ($R^2 = 0.82$). The mean bias under cloud-free conditions was −0.80 kg/m^2 while for all-weather conditions it was −1.25 kg/m^2. Thus, the $SD_{bias}$for all the statistics (temperature, RH and IWV) of the comparison between MWR and RS presented higher values for all-weather conditions than for cloud-free conditions ones. It points out that the presence of clouds is a key factor to take into account when MWR products are used.

The second part of this work is devoted to a seasonal variability analysis over five years, leading us to characterize thermodynamically the troposphere over our site. This city atmosphere presents a clear seasonal cycle where temperature, $ABLH^{max}$ and IWV increase from winter to summer and decrease in autumn, meanwhile RH decreases along the warmer seasons. This city presents cold winters (mean daily maximum temperature: 10.6 ± 1.1 °C) and dry/hot summers (mean daily maximum temperature of 28.8 ± 0.9 °C and mean daily maximum of surface RH up to 55.0 ± 6.0%) at surface (680 m asl). Moreover, considering temporal trends, our study pointed out that only temperature and RH showed a linear increase in winters with a mean-rate of (0.5 ± 0.1) °C/year and (3.4 ± 1.7) %/year, respectively, from ground to 2.0 km agl, meanwhile IWV

* Corresponding author at: Andalusian Institute for Earth System Research (IISTA-CEAMA), University of Granada, Autonomous Government of Andalusia, 18006 Granada, Spain.
E-mail address: aebedoyav@correo.ugr.es (A.E. Bedoya-Velásquez).

https://doi.org/10.1016/j.atmosres.2018.11.014
Received 16 October 2018; Received in revised form 13 November 2018; Accepted 21 November 2018
Available online 22 November 2018

presented a linear increase of 1.0 kg·m^{-2}/year in winters, 0.78 kg·m^{-2}/year in summers and a linear decrease in autumns of −0.75 kg·m^{-2}/year.

1. Introduction

Tropospheric temperature and water vapor content are two key variables for understanding the thermodynamic processes in the atmosphere. Firstly, the knowledge of the thermal structure in the lower part of the atmosphere is a key input for atmospheric boundary layer (ABL) studies (Crook, 1996; de Moreira et al., 2018), for turbulence analysis (O'Connor et al., 2010; Vogelmann et al., 2012), regional climatology and mesoscale numerical models applied on weather forecasting (Stevens and Bony, 2013). Secondly, the water vapor content is directly related to the hydrological cycle, influencing the clouds formation and, therefore, the planetary albedo (Hoff and Hardesty, 2012), and modifying the Earth energy balance at surface. Moreover, the water vapor contribution to the natural greenhouse effect is up to 60% under clear sky conditions, absorbing a significant part of the outgoing infrared radiation (Kiehl and Trenberth, 1997), but also affecting the atmospheric chemical composition and the atmospheric aerosol particles size (Boucher et al., 2013).

Radiosondes (RS) provide in-situ temperature and relative humidity (RH) measurements with high accuracy, precision and vertical resolution. However, their applicability is constrained by several issues: (i) the low frequency of launches; (ii) the air parcel probed might change because of the horizontal wind drift and variable ascent rate during the measurement; (iii) the equipment and man-power costs; and (iv) limitations of measurements under low relative humidity conditions (Vaughan et al., 1988). As an alternative, Raman lidar (RL) systems, based on an active remote technique with high spatial and temporal resolution, can overcome some of the RS drawbacks for measuring water vapor profiles. One of the disadvantages of Raman lidar systems compared to RS is that weather conditions affect the measurements. Besides, these systems need to perform regular calibrations of the water vapor Raman channel by using co-located RS or MWR (Mattis et al., 2002; Guerrero-Rascado et al., 2008a; Navas-Guzmán et al., 2014a, 2014b, Bedoya-Velásquez et al., 2018). In addition, due to the low signal-to-noise-ratio inherent to the RL technique, it is mostly used during night-time. Other methods to retrieve water vapor profiles are based on the synergy between in-situ aircraft and satellite measurements (Stankov, 1998; Löhnert et al., 2004; Delanoe and Hogan, 2008).

Another approach for obtaining these atmospheric profiles is through passive remote sensing techniques. In this sense, the MWR is an instrument that measures the thermal radiation emitted by the atmosphere within 20–200 GHz, operating in continuous mode (24/7) (Rose et al., 2005). Over other techniques, it can provide atmospheric profiles with a high temporal resolution and a reasonable vertical resolution under almost all-weather conditions (Navas-Guzmán et al., 2016). In addition to temperature and RH profiles, the MWR also provides integrated quantities such as integrated water vapor (IWV) and liquid water path (LWP) with high accuracy (Crewell and Löhnert, 2003; Löhnert and Crewell, 2003).

This work presents an analysis of the MWR performance in terms of accuracy and precision by means of a comparison with RS measurements. The mean-bias ($\overline{bias}$) and the standard deviation (SD_{bias}) between MWR and co-located RS have been calculated for the physical temperature and RH profiles, and for IWV. The study also includes the investigation of the MWR performances under all-weather conditions versus cloud-free conditions and daytime versus night-time measurements. After the characterization of the MWR performances, we focused on a tropospheric analysis of the seasonal variability of temperature and RH profiles, IWV and the atmospheric boundary layer height (ABLH) in the city of Granada, a Southern mid-latitude region in Spain, over a period of five years.

The structure of the paper is described as follows. The experimental site and instrumentation is presented in Section 2. Section 3 describes the methodology used to assess the MWR performance and to derive vertically-resolved information on atmospheric thermodynamic properties and ABLH. In addition, it describes the data pre-processing applied in the statistical seasonal study. Section 4 presents the results and discussion of the comparison between MWR and RS measurements and the 5-year statistical analysis of thermodynamics profiles over Granada. Finally, the conclusions are summarized in Section 5.

2. Experimental site and instrumentation

2.1. Experimental site

The data used in this work were collected at the urban station located in the IISTA-CEAMA building (Granada, Spain, 37.16° N, 3.61° W, 680 m asl). The city is located in a natural basin surrounded by mountains with elevations between 1000 and 3398 m above sea level (asl). Near continental conditions prevailing at this site are responsible for large seasonal temperature differences, providing cool winters and hot summers. The diurnal thermal oscillation at surface is quite high throughout the year, often reaching up to 20 °C, and relative humidity is below 40% most of the time. The region is mostly affected in summer by mineral dust particles transported from the North of Africa (Lyamani et al., 2006a, 2006b, 2010, 2012; Guerrero-Rascado et al., 2008b, 2009, 2011; Córdoba-Jabonero et al., 2011; Titos et al., 2012; Navas-Guzmán et al., 2013; Valenzuela et al., 2014; Granados-Muñoz et al., 2016; Benavent-Oltra et al., 2017). Other aerosol sources are mainly produced by traffic, domestic-heating (wintertime) and biomass burning transported from North America, North Africa and the Iberian Peninsula itself (Alados-Arboledas et al., 2011; Navas-Guzmán et al., 2013; Ortiz-Amezcua et al., 2013, 2017; Titos et al., 2017).

2.2. Instrumentation

The main instrument used in this work is the ground-based MWR (RPG-HATPRO G2, Radiometer physics GmbH) (Rose et al., 2005). This is a passive remote sensor, which measures the thermal emission of radiation from the atmosphere in the microwave region. The MWR has a radiometric resolution between 0.3 and 0.4 rms at 1.0-s integration time and a high temporal resolution for vertical profiles, retrieving roughly one profile each two minutes. The MWR has two bands with seven channels each one, the K-band (22–31 GHz) provides information about vertical humidity, making also possible to get information of integrated column products such as IWV and LWP. The V-band (51–58 GHz) contains information about vertical temperature profile (Löhnert and Maier, 2012; Navas-Guzmán et al., 2016), associated to the thermal emission from molecular oxygen in the atmosphere. Water vapor observations are performed at zenith position, while temperature information can be retrieved assuming horizontal homogeneity and performing vertical scanning observations (Löhnert et al., 2009). Vertical profiles of temperature and RH are composed by 39 bins, where 25 are below 2 km of altitude (roughly inside de ABL) with a variable resolution from 10 to 200 m. The vertical resolution in the free troposphere (2 to 10 km) varies from 200 m to 2000 m (the last 14 bins). An absolute calibration is recommended to be performed at least every 6 months, by using cold liquid-nitrogen and hot loads as reference (Turner et al., 2007; Maschwitz et al., 2013). The accuracy of the temperature profile reported by the manufacturer is lower than 0.75 K

RMSE in the range 1.2–4.0 km and larger than 1.0 K RMSE from 4 to 10 km. However, there is no reported accuracy for RH profile, because RH profiles are retrieved from the combination of temperature and absolute humidity profiles. The absolute humidity profiles have an accuracy up to ± 0.02 g/m^3 RMS from 0 to 1 km, up to ± 0.04 g/m^3 RMS above 2 km, and within the boundary layer up to ± 0.03 g/m^3 RMS (i.e. 0–2000 m). MWRs commonly use temperature inversion methods based on neural networks or linear regressions, which requires a long database taken close to the instrument for training them (Cimini et al., 2015), normally, many RSs are used for this aim, becoming it their principal disadvantage. Also, other inversion algorithms based on Optimal Estimation Method (Rodgers, 2000) have been used in the last years to overcome this problem (Bernet et al., 2017; Navas-Guzmán et al., 2014b, 2017). In this work, the manufacturer has performed the training of the MWR inversion algorithm by using neural networks.

RSs are launched from IISTA-CEAMA mainly during field campaigns or specifically for RL water vapor channel calibration (Guerrero-Rascado et al., 2008a; Navas-Guzmán et al., 2014a; Granados-Muñoz et al., 2015; Bedoya-Velásquez et al., 2018). The system used for RS launches is a GRAW DFM-06/09 (GRAW Radiosondes, Germany), which provides profiles of temperature (resolution 0.01 K, accuracy 0.2 K), pressure (resolution 0.1 hPa, accuracy 0.5 hPa) and RH (resolution 1%, accuracy 2%), with vertical resolution depending on the RS ascension velocity, usually around 5 m/s. Data acquisition done by a GRAWmet software and ground station are used. Up to 55 RSs were launched, mainly during summertime, during the five-year period analyzed here (2012–2016).

Additionally, a co-located Sun/sky photometer (Cimel Electronique; CE-318 N) has been used in this study. This instrument belongs to AERONET (Holben et al., 1998), which processes the spectral Sun and sky measurements from the photometer and provides aerosol optical and microphysical properties integrated over the atmospheric column. Aerosol optical depth (AOD_λ) at 380, 440, 500, 675, 870 and 1020 nm are among the AERONET products (https://aeronet.gsfc.nasa.gov). The uncertainty in the retrieved AOD_λ, associated with primary calibration, is 0.01 for visible and infrared wavelengths, while the ultraviolet region has an uncertainty of 0.02 (Holben et al., 1998). In this work, water vapor product from AERONET (level 1.5; version 2) was used as $IWV_{aeronet}$.

Finally, in order to discern clear and cloudy conditions, we have used a cloud cover database obtained from the co-located sky cameras installed on the IISTA-CEAMA roof-top. Cloud cover information from January 2012 to January 2015 was retrieved from the All Sky Imager shown in Cazorla et al. (2008) and Román et al. (2012); while from February 2015 to December 2016 cloud cover was obtained from the SONA sky camera presented in Cazorla et al. (2015) and Román et al. (2017b). A full description of both cameras and methods for each one can be found in Cazorla et al. (2008) and Román et al. (2017a).

3. Methodology

3.1. Assessment of MWR versus RS

In order to characterize the accuracy and precision of the physical temperature and RH profiles from the MWR, a statistical analysis based on the comparison with RS has been done. During this 5-year period, simultaneous measurements of RS and MWR were available, with a total of 55 RS launches of which 23 RS were launched under cloud-free conditions. Thus, the comparison was done by means of the $\overline{bias}$ (Eq. 1), which was interpreted as the accuracy of the MWR measurements,

$$\overline{bias}(z) = \frac{1}{N}\left[\sum_{i=1}^{N}\left(MWR_i(z) - RS_i(z)\right)\right] \quad (1)$$

and the standard deviation (SD) (Eq. 2), that provided information about the precision of the MWR,

$$SD_{bias}(z) = \sqrt{\frac{\sum_{i=1}^{N}\left(bias_i(z) - \overline{bias(z)}\right)^2}{N-1}} \quad (2)$$

Where ?? is the altitude and N is the total data-samples. In order to perform the comparison between RS and MWR profiles, all RS measurements were degraded to the MWR spatial resolution, which has a lower vertical resolution, and the MWR profiles were 30 min-averaged after the RS launch time.

For analyzing the error in the IWV product of MWR, considering RS as reference, the relative mean-bias error (MBE) calculation was performed, as follows:

$$MBE = \frac{1}{N}\sum_{i=1}^{N}\frac{IWV_{MWR_i} - IWV_{RS_i}}{IWV_{RS_i}} \quad (3)$$

The criteria defined for classifying cloud-free conditions days was based on two flags. Firstly, we used the cloud cover from sky camera database assuming cloud cover ≤ 1.0 oktas as cloud-free conditions. Secondly, we defined a threshold by the observation of the LWP and by checking the cloud base height from MWR, finding a representative threshold of LWP for cloud-free days ≤ $40 g/m^2$. In addition, we used the MWR rain flag provided by the manufacturer to exclude rainy days from database.

The MWR performance for IWV was also characterized by means of the mean bias error and also calculating the correlation between the IWV from MWR and the integration of the water vapor mixing ratio (r (z)) derived by RS from 0 to 10 km (without degradation of spatial resolution of the RS). This evaluation was also performed for cloud-free conditions and all-weather conditions classification.

A classification was performed only for cloud-free conditions between daytime and night-time, considering daytime the measures which were obtained under sunlight presence and night-time measures under absence of sunlight, according to the seasons, resulting in 11 comparison cases during daytime and 12 comparison cases during night-time.

3.2. Calculation of ABLH by using microwave radiometer

The algorithm used for the ABLH determination using MWR measurements is described in detail in de Moreira et al. (2018). This algorithm combines two methodologies: the parcel method (PM) and the temperature gradient method (TGM), which are based on the vertical temperature (T(z)) and potential temperature profiles (θ(z)) obtained from MWR by using the definition proposed in Stull, 2011

Thus, the θ(z) was analyzed in order to classify the atmospheric conditions as stable or unstable. This analysis was performed by the comparison of the surface potential temperature (θ(z_0)) with all points in the θ(z) profile below 5 km. The situation was classified as stable if all θ(z) data points had values larger than θ(z_0) and thus, TGM is applied. Otherwise, the condition was classified as unstable and, therefore, PM is used.

The PM assumes the ABLH as the height z where the θ(z) is equal to surface potential θ(z_0), because z is the altitude where an air parcel with ambient temperature (T) can rise adiabatically from the ground by convection (Holzworth, 1964). Such method is applicable only under unstable situations, i.e. inside a convective boundary layer.

The TGM (Stull, 1988) detects the ABLH in stable situations based on two definitions. Firstly, the surface-based temperature inversion, meaning that TGM detects the first height z where T decrease as a function of altitude. Secondly, the top of the stable boundary layer, meaning that TGM finds the first height where $^{d\theta}/_{dz} = 0$.

The first step is to detect the altitude z where the surface-base temperature inversion is situated (from T profile). Then, from z is found the top of stable boundary layer in the θ(z). If surface-base temperature inversion or top of stable boundary layer is not found, the ABLH is classified as “not identified”.

3.3. Statistical seasonal study

The total of measures performed are presented in Table 1, reaching up around one of million profiles measured with MWR over the whole five-years period, separating the calibration days and periods with data absence mainly associated to maintenance of the instrument. For this seasonal statistical study, we defined the seasons by months as follows: winter (December, January and February), spring (March, April and May), summer (June, July and August) and autumn (September, October and November). Here, we performed an hourly-average for each season of every year evaluated in order to have mean-seasonal-behavior from 0 to 24 h to determine the seasonal diurnal cycle (vertical behavior for temperature and RH, and columnar integrated behavior for IWV), adding the results of the mean $ABLH^{max}$. Then, we divided the atmosphere in nine probed volumes: H1 (bins: 1–14, from 0 to 0.55 km agl), H2 (bins: 15–19, from 0.6 to 1.0 km agl), H3 (bins: 20–22, from 1.2 to 1.5 km agl), H4 (bins: 23–25, from 1.6 to 2.0 km agl), H5 (bins: 26–29, from 2.2 to 3.1 km agl), H6 (bins: 30–32, from 3.5 to 4.4 km agl), H7 (bins: 33–35, from 5.0 to 6.2 km agl), H8 (bins: 36–37, from 7.0 to 8.0 km agl),H9 (bins: 38–39, from 9.0 to 10.0 km agl), in order to look for the seasonal variability of the median of the temperature and RH within the different tropospheric regions. In addition, we also used the median-seasonal trend of PW along the five years took from NASA AERONET level 1.5 level data for the Granada station to support some of the results obtained.

4. Results and discussion

4.1. Characterization of MWR performances versus RS

Fig. 1 presents the ($\overline{bias}$ and SD_{bias}) between MWR radiometer and RS for temperature and relative humidity under clear and all-weather conditions. These two statistic parameters are interpreted as the accuracy and the precision, respectively, of the MWR measurements. Fig. 1a shows high variability of the temperature $\overline{bias}$ for all-weather conditions mostly in the first hundreds of meters, passing from positive to negative values. The larger deviations observed close to ground have been observed in similar comparisons for previous studies and could be due to the larger uncertainties of the radiative transfer models for the most transparent MWR channels, which affect more the temperature retrievals in the lowest layers (Navas-Guzmán et al., 2016). In general, below 2.0 km agl, the variability shows low-temperature $\overline{bias}$ values from 1.7 to −0.4 K. The variability starts to increase from negative to positive within 2.0 to 4.0 km agl (up to 1.0 K). This $\overline{bias}$ increases up to 1.8 K above 4.0 km agl, indicating the losing of accuracy with altitude always with positive values. The SD_{bias} of the temperature deviation profiles in all-weather conditions shows values lower than 3.0 K below 2.0 km agl, increasing up to 3.2 K from 2.0 to 4.0 km agl, and keeping constant close to 3.0 K from 4 to 7 km agl. The cloud-free conditions analysis shows the same variability in the mean bias within the first hundreds of meters than the one observed for all-weather conditions, after this region the $\overline{bias}$ changed from positive to negative values, oscillating from 1.8 to −0.4 K (below 2.0 km agl). Then, between 2.0 and 4.0 km agl, the bias pass from negative to positive. Above 4.0 km agl some variability lower than 1.7 K, indicating the losses of the accuracy as altitude increases. The temperature SD_{bias} profile under cloud-free conditions presents values lower than 1.1 K from ground to 2.0 km agl, while they increase (up to 1.8 K) for higher altitudes. It is important to point out the lower SD_{bias} values observed under cloud-free conditions, indicating a higher precision of temperature MWR measurements under clear conditions than for all-weather conditions.

In addition, the surface heating caused by solar radiation tends to increase the variability of the temperature profiles over the firsts kilometers of the troposphere (up to 3.0 km agl). Above this altitude the atmosphere becomes cooler and the SD_{bias}profiles becomes quite constants.

The same analysis was performed for RH under all-weather conditions and cloud-free conditions (Fig. 1b). Under all-weather conditions, the RH $\overline{bias}$ profile shows relatively low deviations, passing from positive values (from surface to 1.6 km agl) to negative (from 1.6 until 2.0 km agl) (from 3 to −4.0%). The RH $\overline{bias}$ becomes greater (up to −18.0%) from 2 to 4 km agl; then above 4 km agl reach up −11.0%. The SD_{bias} ranges from 10 to 16.3% from ground to 2 km agl, above this altitude it presents a variation from 15 to 21.0% (from 2 to 4 km agl).Then, it decrease from 4 to 7 km agl from 21 to 17%. Cloud-free conditions $\overline{bias}$ profile has a similar behavior below 2 km agl (ranging from 2.0 to −4.0%), then increasing up from −4.0 to −21.4% until 4 km. Finally, a decrease is seen to −4.5% from 4 to 7 km agl. Regarding SD_{bias}-RH profile in cloud-free conditions, from ground to 2 km agl the discrepancy was ranging from 0.5 to 13.3%, increasing from 2to 3.0 km agl up to 19.3%, then decreasing up to 15% until 4.0 km agl. From 4.0 km agl to the top of the profile, decreasing until 9.3%. This losing of precision, mostly between 2 and 4 km agl, might be associated to the method for retrieving the RH profiles. This type of profile lose accuracy above the ABL, mainly because at this altitudes the absolute humidity is typically quite low (due to the low temperatures) becoming very difficult a proper detection of this property by microwave radiometry and, therefore, the RH retrievals loose precision. The SD_{Bias}-RH profile of all-weather conditions presents higher variability respect to cloud-free conditions, showing a difference around 5% over almost all the profile, which might be associated to the cloud presence.

Summarizing this inter-comparison, it is worth to point out that temperature profiles obtained from MWR makes an underestimation of those taken by RS just between 1.5 and 2.3 km agl, the profile below 1.5

Table 1
MWR measurements over five-years at Granada station, reporting for each year the total of days (D) and profiles (P) measured by month.

Year	2012		2013		2014		2015		2016	
Month	D	P	D	P	D	P	D	P	D	P
January	31	12648	31	12648	20	14400	5	3600	28	20160
February	29	11832	28	11424	28	20160	28	20160	29	20880
March	31	12648	31	12648	31	22320	31	22320	11	7920
April	30	12240	30	12240	11	7920	30	21600	26	18720
May	31	12648	8	5760	20	14400	16	11520	31	22320
June	30	12240	30	21600	30	21600	0	0	24	17280
Juli	31	12648	31	22320	21	15120	18	12960	31	22320
August	31	12648	31	22320	31	22320	31	22320	31	22320
September	30	12240	30	21600	30	21600	30	21600	17	12240
October	31	12648	31	22320	16	11520	27	19440	31	22320
November	30	12240	24	17280	30	21600	30	21600	25	18000
December	31	12648	14	10080	15	10800	30	21600	0	0
TOTAL	366	149328	319	192240	283	203760	276	198720	284	204480

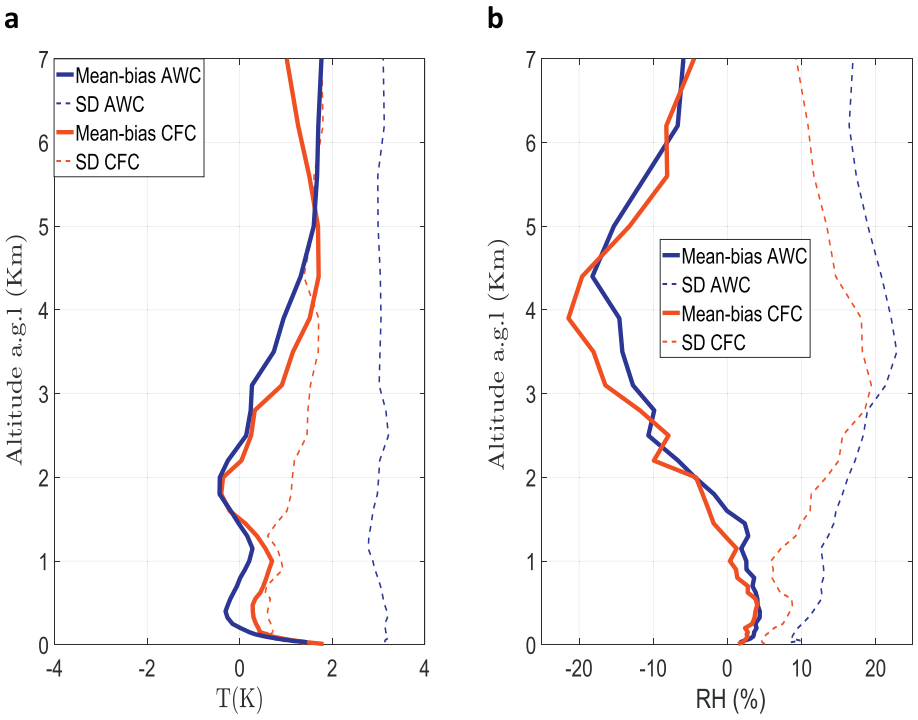

Fig. 1. Mean bias (solid line) and standard deviation (dashed line) on all-weather conditions (AWC, blue) and cloud-free conditions (CFC, red) for temperature (a) and RH (b) profiles between RS and MWR. (For interpretation of the references to colour in this figure legend, the reader is referred to the web version of this article.)

and above 2.3 km agl presented an overestimation. The RH $\overline{bias}$ profile exhibits an overestimation below 1.5 km agl, but above this altitude, an underestimation of the RH profiles is seen from MWR respect to the obtained for RS.

In order to characterize the performance of MWR to retrieve IWV (IWV_{MWR}), an integration of the r (z) profile calculated from RS was performed to derive IWV_{RS}. Fig. 2 shows the scatter plot between IWV_{MWR} and IWV_{RS}. The fit for cloud-free conditions shows a slope closer to one (0.85 ± 0.03) and a better determination coefficient ($R^2_{CFC} = 0.96$) than all-weather conditions (slope = 0.68 ± 0.03, $R^2_{AWC} = 0.82$), which determines that cloud-free days fit better. This fact is associated to the vertical and horizontal homogeneity that atmosphere presents under cloud-free conditions, which is not seen for RS and MWR measurements under cloud presence, evidencing high data dispersion in all-weather conditions (moving away to the 1:1 line). The MBE is also calculated to reinforce the fact that all-weather conditions introduce large errors respect to cloud-free conditions measurements, showing a MBE to cloud-free conditions up to $-0.80\ kg/m^2$, meanwhile for all-weather conditions the MBE is up to $-1.25\ kg/m^2$. As seen in Fig. 2, the cloud presence introduces high data-dispersion, weakening the correlation.

The performance of the MWR has also been analyzed distinguishing between daytime and night-time measurements (Fig. 3), but only for cloud-free conditions since it is the scenario with better performance. The temperature $\overline{bias}$ is up to 2.0 K reached in the first hundreds of meters, which is the region with higher variability. Above that, a positive temperature $\overline{bias}$ is observed below 1.8 km agl, ranging from 0.7 to 1.0 K for daytime and from 0.5 to 0.6 K until 1.5 km agl for night-time, showing lower variability during night-time because of the sunlight absence. The $\overline{bias}$ becomes negative from 1.8 to 3.5 km agl (up to −0.5 K) for daytime and from 1.5 to 2.3 km agl (up to −0.5 K) to night-time. The $\overline{bias}$ becomes positive above 3.5 km agl reaching 1.7 K for daytime and 1.8 K above 2.3 km agl for night-time. The SD_{bias} analyzed under the same three ranges of altitude, presented lower values for daytime close to 0.6 K, 1.3 K and 1.7 K than night-time 1.0 K, 1.2 K and 2.0 K, in fact the night-time is relatively more variable under the first 2 km agl, maybe associated to the thermal inversions during the night.

The same behavior is also seen on RH $\overline{bias}$-profile where the daytime profile is more variable within the first 1.5 km agl (up to 8%) than night-time one (up to 2%), which is almost constant in the first 1.5 km. The variability at daytime is mostly associated to the Sun presence, because the temperature modifies the water vapor pressure. From this altitude until 4.5 km agl for daytime and 5.5 km agl at night-time, the RH $\overline{bias}$ becomes negative decreasing up to −26.5% and −16.8%, respectively. From 4.5 to 7 km agl for daytime and night-time from 5.5 to 7 km agl, the RH mean-bias decreased to −8.1% and −8.4%, respectively. RH-SD_{bias} presented the following values according to the altitude ranges exposed above, for daytime from 6 to 8.8% (up to1.5 km agl), up to 23.5% (up to 4.5 km agl) and decreasing to 18.3% (up to7 km agl), while night-time variates from 5 to 10.0% (within 1.5 km agl), increasing to 20.0% (up to 4.5 km agl) and it starts to descend up to

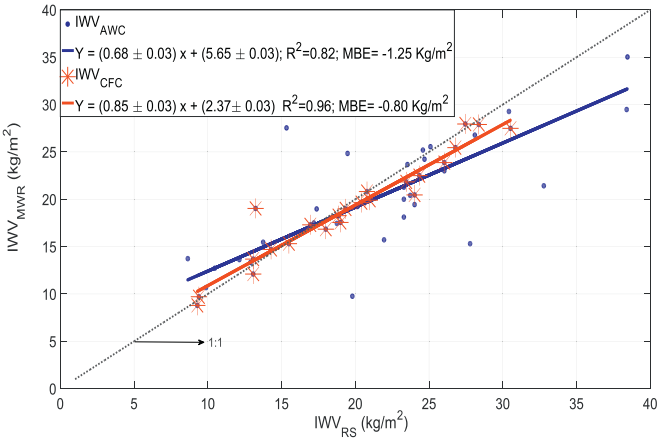

Fig. 2. IWV from MWR versus RS for all-weather conditions (AWC, in blue) and cloud-free conditions (CFC, in red). The gray dashed-line refers to 1:1 line. (For interpretation of the references to colour in this figure legend, the reader is referred to the web version of this article.)

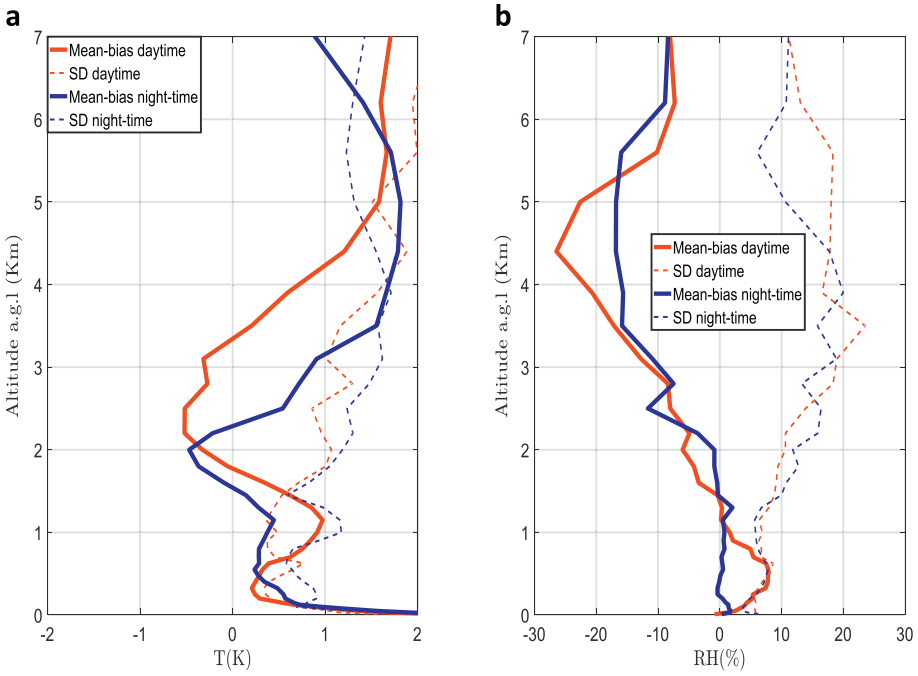

Fig. 3. Mean bias (solid line) and standard deviation (dashed line) on daytime (red) and night-time (blue) for T (a) and RH (b) profiles between MWR and RS, all for cloud-free conditions (CFC). (For interpretation of the references to colour in this figure legend, the reader is referred to the web version of this article.)

11.1% at 7.0 km agl. From this analysis, we can point out that the MWR present quite good performance for RH in the first two kilometers, with mean bias and SD_{bias} lower than 10%. Above 2 km (agl) these profiles should be used more carefully, taking into account that error might be as high as 20%, affecting strongly the calculations performed.

4.2. Statistical analysis of five-year of MWR measurements

4.2.1. Diurnal cycle analysis

In order to investigate the diurnal cycle of the temperature and RH profiles in the troposphere, the hourly-mean cycle for temperature and RH profiles is analyzed for each season and every year from 2012 to 2016 (Figs. 4 and 5, respectively). To complete the study, $ABLH^{max}$ retrievals have been included. Fig. 4 shows the hourly-mean behavior of

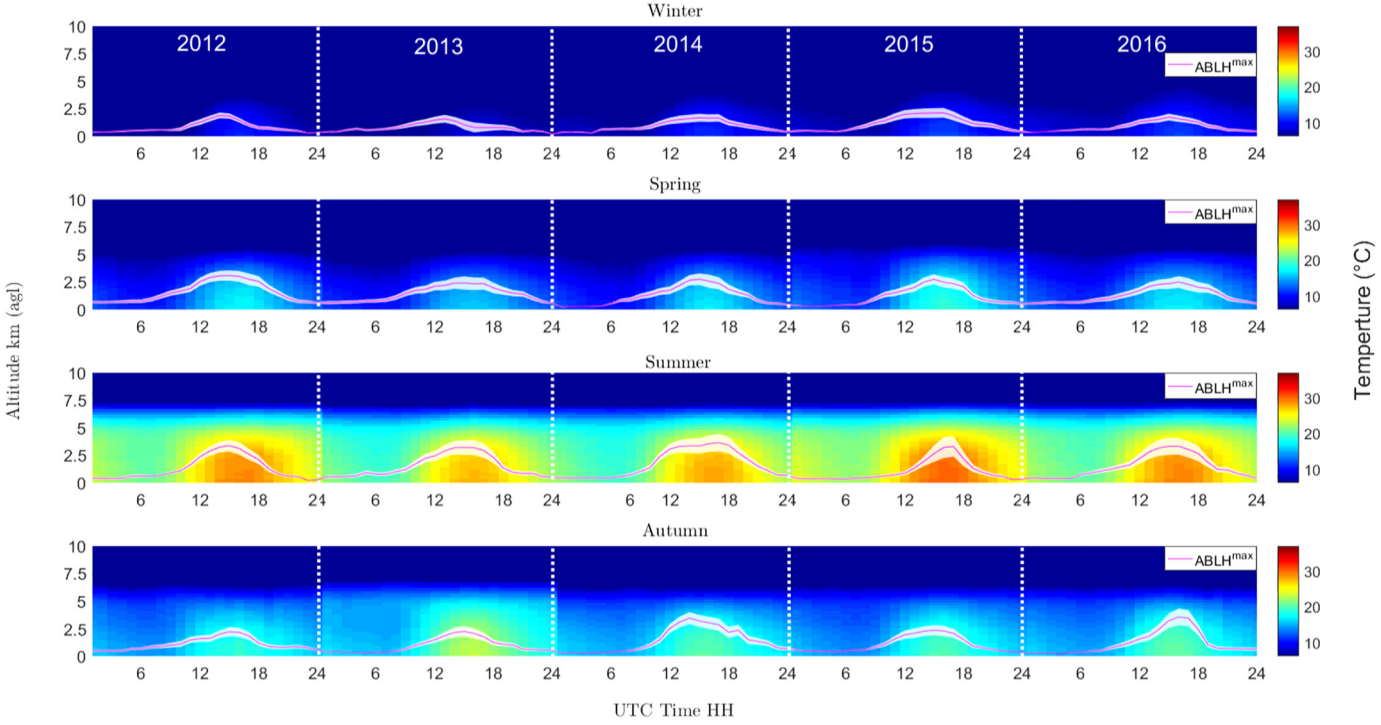

Fig. 4. Mean 24-h cycle for temperature profiles and ABLH by season and year. The magenta line refers to the mean $ABLH^{max}$ and the white contour is the SD. (For interpretation of the references to colour in this figure legend, the reader is referred to the web version of this article.)

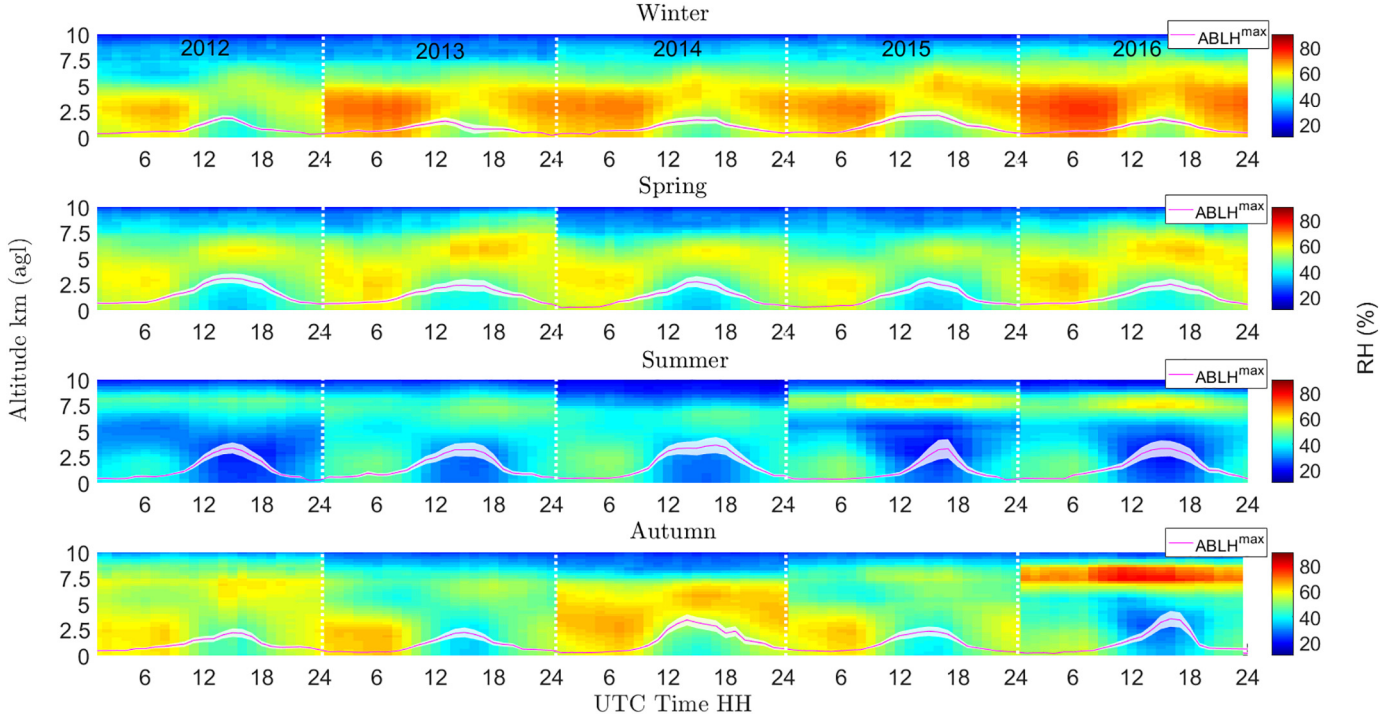

Fig. 5. Mean 24-h cycle for RH profiles and ABLH by season and year. The magenta line refers to the mean ABLH^{max} and the white contour is the SD. (For interpretation of the references to colour in this figure legend, the reader is referred to the web version of this article.)

the temperature profiles, where we can see that the maximum effect of the solar irradiation at surface level is close to 16 UTC and the minimum around 7 UTC, variating slightly depending of the season. In addition, due to the solar heating of the surface, the lowermost troposphere is heated with a variable vertical extension, reaching up to 6 km agl in summer, and up to 5 km agl in autumn, becoming lower in winter (up to 2 km agl) and spring (up to 4 km agl). This effect mainly drives the evolution of the mean-ABLH, which is a crucial parameter for studying aerosol dynamics and air masses transport (de Moreira et al., 2018).

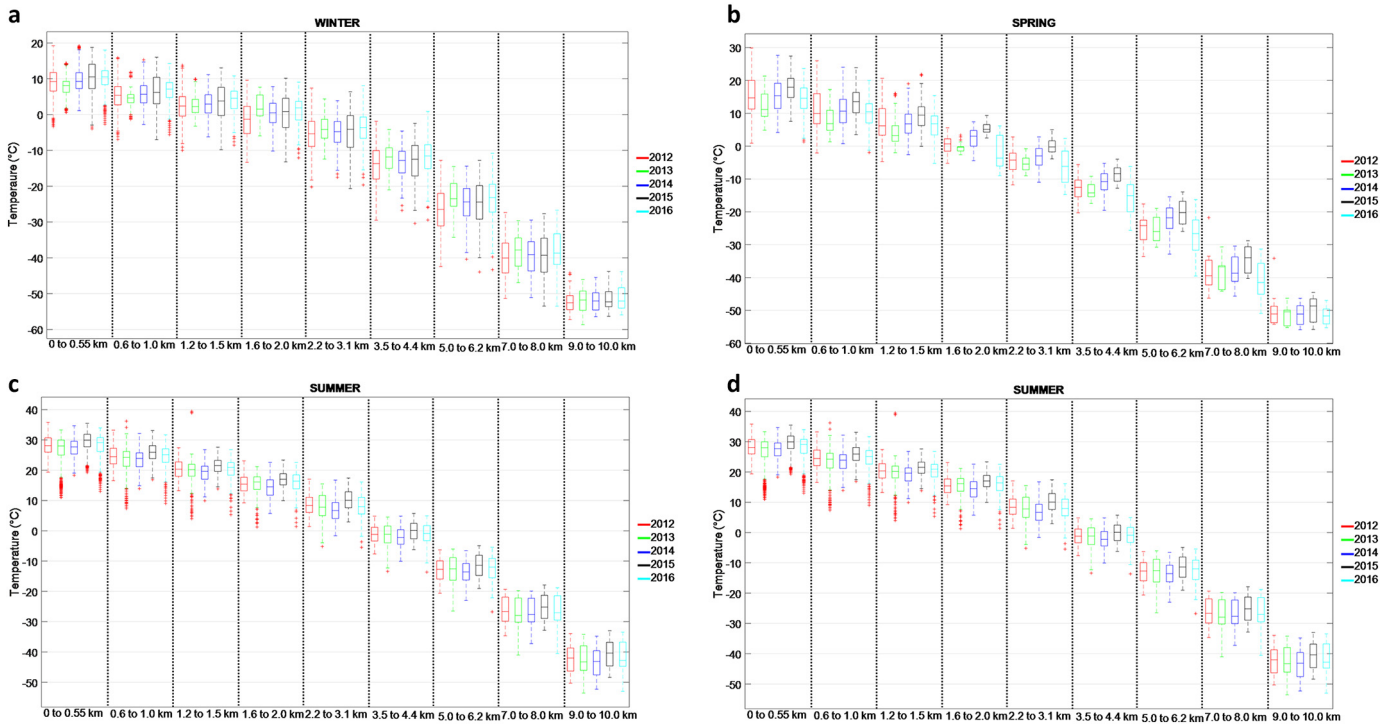

Fig. 6. Seasonal boxplots of temperature presented for nine atmospheric volumes covering the 39 bins of the MWR for the years 2012 (red), 2013 (green), 2014 (blue), 2015 (black) and 2016 (cyan). Winter (panel a), spring (panel b), summer (panel c), and autumn (panel d). In the boxes are represented the 25 and 75 percentile, the median, the maximum and minimum, and the outliers marked with asterisks. (For interpretation of the references to colour in this figure legend, the reader is referred to the web version of this article.)

The algorithm implemented for ABLH retrieval presented in Sec. 3.2 allows us to retrieve the altitude where temperature profile evidences an abrupt change under stable or unstable atmospheric conditions. Thus, the mean-ABLH^{max} presented on Fig. 4, increases gradually from winter (~ 2.1 km agl) to summer (~ 3.7 km agl), because of the increasing in solar incoming radiation that reaches the Earth's surface. In autumn, the mean-ABLH^{max} starts to decrease (~ 2.2 km agl), in agreement with the ABL studies reported by de Moreira et al., 2018over this area. ABLH^{max} starts to increase lately in the morning in winter (~ 7 UTC), meanwhile summer exhibits faster increase up from 6 UTC, associated to the incoming solar insolation that begins earlier to warm up the surface.

Fig. 4 determines that the warmest year of this study was 2015,with mean values at 16 UTC up to 11.6 ± 4.0 °C, 19.0 ± 4.1 °C and 30.0 ± 1.8 °C at surface level in winter, spring and summer, respectively. Autumn was an exception, becoming autumn 2013 the warmest in the period 2012–1016, with mean-maximum temperature of 23.1 ± 5.7 °C. The coldest mean values at ground level by season were reached in winter 2012 (10.5 ± 3.5 °C), spring 2013 (15.6 ± 7.6 °C), summer 2013 (27.5 ± 2.1 °C) and autumn 2012 (19.2 ± 6.4 °C).

Fig. 5 presents the same analysis for RH, where the hourly-mean maximum values for the RH profile at surface level are observed close to 7 UTC. This is consistent with the lower temperature values, since the diurnal cycle between temperature and RH is opposite. The intervals with higher RH are in late night and mornings (from 2 to 10 UTC) and night (from 21 to 24 UTC), where solar heating is weaker or absent. In the mornings, RH presents high values at surface level (winter ~ 80%, spring ~ 65%, summer ~ 50% and autumn ~ 62%). These values tend to increase with altitude until 4 km agl in winter, spring and autumn, but in summer reaches up to 3 km because of higher temperatures. In the late afternoons, this value may be little lower at surface reaching up in winter ~ 70%, spring ~ 55%, summer ~ 40% and autumn ~ 60%, experimenting the same increase with altitude until 4 km agl depending of the season. The driest region observed in the RH profiles at surface level is close to 16 UTC, and it reaches in winter ~ 60%, spring ~ 48%, summer ~ 28% and autumn ~ 35%. This region can reach 5 km agl or more in spring and summer becoming lower in winter and autumn. As we shown in Section 4.1, the RH mean-bias profiles above 2 km agl, losses accuracy and precision, therefore the results above this altitude have larger uncertainties.

From Figs. 4 and 5, it is detected a clear seasonal cycle in temperature, RH and ABLH^{max}, governed by solar radiation. Granada is characterized by cold winters (mean hourly maximum temperature at surface of 10.6 ± 1.1 °C) and warmer summers (mean-hourly maximum of 28.8 ± 0.9 °C). In summer, RH at surface can be as low as 18.5 ± 1.9% (mean-hourly minimum value) in the driest part of the day and in the mornings where humidity is higher; it could reach a mean-hourly maximum of 55 ± 6%, evidencing the dry conditions of this city.

4.2.2. *Statistical analysis of temperature and RH in the vertical coordinate*

In this section, a seasonal variability study of atmospheric variables like temperature and RH in altitude and IWV in column is presented. Fig. 6 shows the temperature boxplots by year and season. In addition, we divided the profile by nine bins to cover the whole troposphere as was describe in section 3.3, allowing us to investigate effects inside the low troposphere, which is directly linked with ABL (typically from 0 to 3 km agl) and middle and high troposphere (from 3 km agl to 10 km agl). Accordingly, to the results obtained in Section 4.2.1, we are only interested on studying when temperature exhibits their maximum value along the day over all seasons (RH behaves oppositely); therefore, this statistical analysis will be performed at 16 UTC. Around this hour, the ABL is fully developed and the atmosphere is good mixed.

Temperature boxplots dataset shows that 25% of the lowest and 25% of the highest temperatures are symmetrically distributed respect to the median value showing low data dispersion for most of height-ranges evaluated. In general, all seasons presented in 2013 smaller boxes than the other seasons, mostly between H1 to H4. Fig. 6 presents that outliers are more frequent within H1 to H5, increasing in summer, associated to the increase of the variability caused by high temperatures

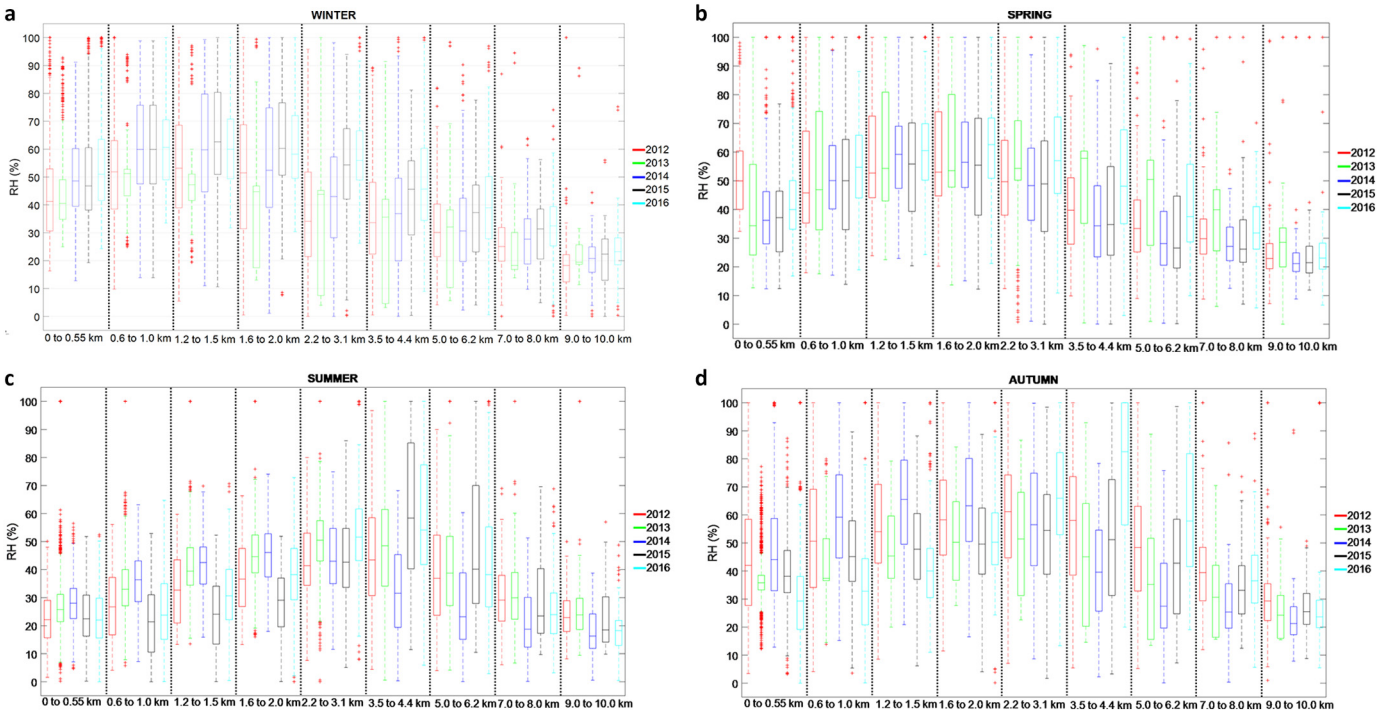

Fig. 7. Seasonal boxplots of RH presented for nine atmospheric volumes covering the 39 bins of the MWR for the years 2012 (red), 2013 (green), 2014 (blue), 2015 (black) and 2016 (cyan). Winter (panel a), spring (panel b) summer (panel c) and autumn (panel d). In the boxes are represented the 25 and 75 percentile, the median, the maximum and minimum, and the outliers marked with asterisks. (For interpretation of the references to colour in this figure legend, the reader is referred to the web version of this article.)

within ABLH.

RH boxes (Fig. 7) are quite larger than temperature pointing a higher data dispersion. In addition, RH shows much more outliers (both above and below the boxes), mainly associated to (i) the cloud presence and (ii) the decrease of the absolute humidity with altitude, making less accurate the radiometric measures. This fact makes that MWR retrievals present higher or lower values than real measurements above 2.0 km agl, producing more outliers. RH presents a trend to increase from H1 to H3 and decreasing from H4 to H9 for winter, spring and autumn. This trend is broke up in summer when this increase reaches higher altitudes (from H1 to H6), and decreases from H7 to H9.

In general, IWV data boxplots presented in Fig. 8 exhibit less data-dispersion. The distribution of the data shows high equilibrium below 25% and above 75%, meaning that values are relatively well distributed around the median with lower data outliers. This variable presents a seasonal trend to increase from winter to summer and decreasing in autumn, showing their high relation with temperature seasonal trend.

4.2.3. Inter-annual trend analysis by season

Table 2 reports for each season the inter-annual trend of temperature and RH computed by means of the calculation of the linear fits of the median values registered. Temperature only exhibits an inter-annual increase from H1 to H7 in winter season, from 0 to 1.0 km agl, increased between 0.4 and 0.6 °C/year, depending on the height range. Thus, winters in Granada are becoming warmer, mostly within the first 2.0 km agl. With a weaker correlation ($R^2 = 0.44$), summers exhibit an increase of 0.4 °C/year only close to surface (H1). The rest of the seasons do not present a clear inter-annual trend, with determination of R^2 coefficients below 0.50 for all height-ranges.

The results of the inter-annual increase of temperature are in agreement with climatological studies performed at Iberian Peninsula by Río et al. (2011) and Coll et al. (2017), reporting a surface temperature increasing trend in winter in the South and South-Eastern of the peninsula, where Granada station presented the drier conditions in the southern region of the peninsula. The results obtained here presents higher values for the inter-annual trend of temperature respect to those reported in literature, mainly because the instrumentation involved, the dataset size and the statistical techniques used in the datasets. Moreover, the inter-annual temperature increases in winter season reported in this study are also in agreement to the report of CALIMA (Caracterización de Aerosoles originados por Intrusiones de Masas de aire Africanas, *characterization of African air masses outbreaks,* http://www.calima.ws/episodiosocurridos.html), which is a program in charge to quantify the Saharan dust events over Iberian Peninsula. Its record indicates that from 2013 to 2015 the Saharan dust outbreaks have increased their number and become more intense in winter season, mostly within the second fortnight of February.

Regarding RH, winter presents a clearly linear increase for all the altitudes analyzed (note that information at ranges H6-H9 are not included due to the loose of accuracy and precision of the RH retrievals following section 4.1). The highest rates of increasing are in the middle of the troposphere (between H4 and H5, 7.4 and 5.4%/year, respectively). In spring, the RH increases linearly from H2 to H4. In summer and autumn, non-significant inter-annual trend were observed.

Table 3 presents the inter-annual trend of IWV and PW by season. Our computations indicate that IWV is increasing over the years with high correlations in winter ($1.0 \pm 0.1 kgm^{-2}$/year, $R^2 = 0.95$) and summer ($0.8 \pm 0.1 kgm^{-2}$/year, $R^2 = 0.73$), while PW only experimented an increasing trend high correlated (0.07 ± 0.03 cm/year, $R^2 = 0.6$) in winter. This behavior in winter pointed out that every year during our study Granada is becoming more humid; furthermore, the likelihood of precipitations is higher in winter than in the rest of seasons. The IWV in spring presented no-correlation (up to 0.26) due to the higher median value found in 2016 (up to 12.5 kgm^{-2}), this value tends to change the real tendency to decrease of this season (also seen in Fig. 8). If we perform the analysis hiding spring 2016 median data, IWV in spring presents a decreasing tendency with a slope up to $-0.2 kgm^{-2}$/year and $R^2 = 0.80$. The fact of IWV in 2016 becomes higher is not clearly seen in this study, just we could associate to the statistical weight, because in March the percentage of missing data is up to 64.5% (11 days measured), so the median value of the month could affect the seasonal median. IWV in autumn presented a strong correlation ($R^2 = 0.95$) with a linear decrease up to –0.75 kgm^{-2}/year which is not really linked with inter-annual temperature cycle. This analysis showed no-correlation of PW in spring, summer and autumn, however the seasonal trends for both IWV and PW are the same, increasing from winter to summer and decreasing in autumn. The higher values of IWV were reached in spring and summer, mostly associated to the vegetation presence and high temperatures, which increases the evapotranspiration process. Finally, it is important to taking into account the warm air mases that comes from Atlantic Ocean and Mediterranean Sea, with high temperatures, this fact increase the capacity of these air masses to harbor water vapor before saturation.

5. Conclusions

Our analysis over a 5-year dataset of the RPG-HATPRO MWR leaded us to quantify its accuracy and precision by means of the mean-bias and standard deviation for temperature and RH vertical profiles under cloud-free conditions and all-weather condition, and integrated water vapor (IWV) column product. In addition, an analysis of the MWR performances during night- and day-time was carried out under cloud-free conditions. We found that the temperature $\overline{bias}$ profile under all-weather conditions exhibited high confidence, mostly below 2 km agl with values ranging from 1.7 to −0.4 K. The SD_{bias} under all-weather conditions was quite constant in altitude, with values around 3 K in the whole troposphere. Under cloud-free conditions, the mean bias showed quite similar values than under all-weather conditions, although some differences were found in the lowest layer (below 1.5 km) and between 3 and 5 km (agl), where the mean bias was slightly higher under cloud-free conditions reaching up 1.8 K. An important point to be remarked is the lower SD_{bias} that was observed under cloud-free conditions. The SD_{bias} profile presented values ranging between 1.1 and 1.8 K in the whole troposphere, indicating a higher precision of the MWR under these conditions.

The performance for RH under all-weather conditions showed from surface to 2 km agl that $\overline{bias}$ was ranging from 3.0 to −4.0% with SD_{bias} between 10 and 16.3%, and from 2 to 4 km the $\overline{bias}$ was up to −18%

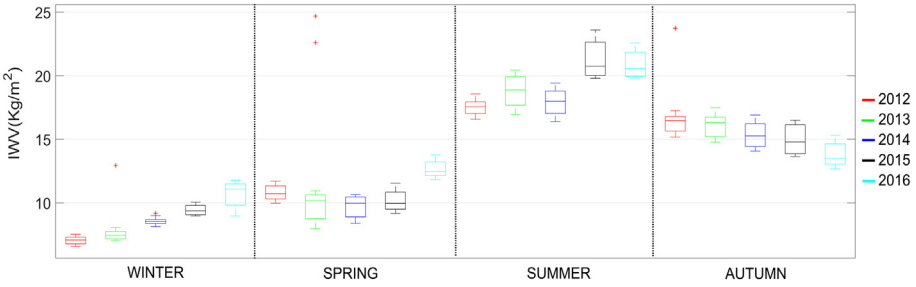

Fig. 8. Seasonal boxplots of IWV the years 2012 (red), 2013 (green), 2014 (blue), 2015 (black) and 2016 (cyan). The line within the box refers to the median value, and the top and bottom of the box are the 75 and 25 quartiles, respectively. The outliers are marked with a red cross symbol. (For interpretation of the references to colour in this figure legend, the reader is referred to the web version of this article.)

Table 2
Inter-annual trends of temperature and RH by season and height-range. Where W (winter), S (spring), SU (summer) and A (autumn).

		H1	H2	H3	H4	H5	H6	H7	H8	H9	
T (K)	Slope (°C/year)	0.5 ± 0.6	0.5 ± 0.5	0.6 ± 0.3	0.6 ± 0.5	0.4 ± 0.8	0.4 ± 0.8	0.6 ± 0.5	0.1 ± 1.8	0.1 ± 3.1	W
	R^2	0.60	0.73	0.90	0.52	0.70	0.50	0.50	0.06	0.06	
	Slope (°C/year)	0.7 ± 0.3	0.8 ± 0.3	0.8 ± 0.3	−0.3 ± 0.3	0.1 ± 0.4	0.1 ± 0.3	0.1 ± 0.3	−0.2 ± 0.3	0.1 ± 0.8	S
	R^2	0.18	0.26	0.29	0.001	0.01	0.001	0.001	0.01	0.01	
	Slope (°C/year)	0.4 ± 0.7	0.3 ± 0.9	0.3 ± 1.1	0.3 ± 0.8	0.2 ± 0.7	0.2 ± 1.0	0.3 ± 1.0	0.2 ± 0.8	0.1 ± 0.7	SU
	R^2	0.44	0.36	0.28	0.22	0.001	0.12	0.24	0.01	0.03	
	Slope (°C/year)	0.3 ± 0.5	0.4 ± 0.4	0.1 ± 0.5	−0.3 ± 0.7	−0.2 ± 0.7	−0.3 ± 0.7	−0.3 ± 0.6	−0.3 ± 0.6	−0.4 ± 0.5	A
	R^2	0.01	0.08	0.01	0.20	0.10	0.16	0.15	0.11	0.18	
RH (%)	Slope (%/year)	2.6 ± 0.1	2.6 ± 0.1	2.9 ± 0.1	7.4 ± 0.1	5.42 ± 0.03	–	–	–	–	W
	R^2	0.79	0.77	0.54	0.56	0.91	–	–	–	–	
	Slope (%/year)	−1.7 ± 0.1	2.1 ± 0.1	1.7 ± 0.2	2.1 ± 0.1	0.9 ± 0.2	–	–	–	–	S
	R^2	0.19	0.91	0.68	0.76	0.15	–	–	–	–	
	Slope (%/year)	−0.4 ± 0.3	−1.7 ± 0.1	−2.0 ± 0.1	−1.2 ± 0.1	1.3 ± 0.2	–	–	–	–	SU
	R^2	0.04	0.19	0.18	0.08	0.17	–	–	–	–	
	Slope (%/year)	−2.3 ± 0.1	−2.8 ± 0.1	−2.6 ± 0.1	−1.7 ± 0.1	1.3 ± 0.2	–	–	–	–	A
	R^2	0.40	0.17	0.17	0.18	0.12					

Table 3
Inter-annual trend of IWV and $IWV_{aeronet}$ by season in the period 2012–2016.

	Slope (kgm-2/year)	R^2	Season
IWV_{MWR} (kgm^2)	1.0 ± 0.1	0.95	Winter
	0.3 ± 0.7	0.26	Spring
	0.8 ± 0.1	0.73	Summer
	−0.8 ± 0.2	0.95	Autumn
$IWV_{aeronet}$ (cm)	0.07 ± 0.03	0.60	Winter
	0.01 ± 0.05	0.02	Spring
	0.03 ± 0.03	0.30	Summer
	−0.03 ± 0.04	0.20	Autumn

with SD_{bias} ranging between 15 and 21%. Above 4 km the $\overline{bias}$ reached up to −11.0 with SD_{Bias} ranging from 12 to 17%. The same altitudes ranges were evaluated under cloud-free conditions showed high confidence within the first 2 km ranging from 2.0 to −0.4 with SD_{bias} from 0.5 to 13.3%, then from 2 to 3 km agl were up to −4.0 to −21.4 with SD_{bias} 19.3%, and decreasing up to −4.5% with SD_{bias} 9.3%. The temperature and RH SD_{bias} showed a positive offset close to 2.5 K and 5%, respectively, between all-weather conditions and cloud-free conditions, associated with cloud presence. Finally, a performance of the IWV product allowed us to see the effect of the cloud presence over this product. Thus, the determination coefficient was up to 0.82 for all-weather conditions, meanwhile it increases up to 0.96under cloud-free conditions The MBE was lower for all-weather conditions (−0.80 kg/m^2) than cloud-free conditions (−1.25 kg/m^2).

The cloud-free conditions database (temperature and RH) was investigated under daytime and night-time scenarios. This classification exhibits a time-dependency associated to the solar heating on the surface, becoming more variable during daytime respect to night-time. The temperature $\overline{bias}$ profile was ranging from 0.7 and 1.0 K with SD_{bias}up to 1.0 K agl at daytime below 1.8 km agl and from 0.5 to 0.6 K at night-time with SD_{Bias}0.6 K below 1.5 km. This error increase with altitude. The RH also presents low errors below 1.5 km agl up to 8% at daytime with SD_{bias} ranging from 6 to 8.8% and up to 2% with SD_{bias} ranging from 5 to 10% at night-time. After this altitude, the accuracy and precision increase rapidly with height.

The results obtained here allows to assess the reliability range of the HATPRO MWR G2 system, in order to use products like temperature, RH and IWV in further applications like foresting models, ABL studies, and aerosol hygroscopic growth, among others at this mid-latitude region.

The second part of this work was focused on a statistical study over a 5-year dataset. Firstly, it was observed that temperature, IWV and $ABLH^{max}$ daily-seasonal cycle presents an increasing trend from winter to summer, decreasing in autumn, meanwhile RH daily-seasonal cycle is opposite, maximum in winter decreasing until summer and then increasing again in autumn; all of them governed by the solar radiation. The maximum temperature values were around 16 UTC coinciding with the minimums RH values, instead RH maximums are located from 2 to 10 UTC and from 21 to 24 UTC. The hourly- mean cycle leading us to conclude that 2015 was the warmest year for all seasons, except in autumn 2013 that showed up an abruptly increase of temperature respect to other years. The coldest seasons do not follow a yearly pattern, becoming the coldest winter 2012, spring 2014, summer 2014 and autumn 2015. The highest RH values were found in winter 2016, spring 2016, summer 2015 and autumn 2016; and the lowest RH values in winter 2012, spring 2014, summer 2014 and autumn 2014. Finally, the inter-annual study is linked with seasonal, pointing out that temperature and RH showed up an inter-annual linear increase in winter with a mean-trend up to (0.5 ± 0.1) °C/year and (3.4 ± 1.7) %/year, respectively, from ground to 6 km agl. IWV presented an inter-annual linear increase up to 1 kgm^{-2}/year in winter and 0.78 kgm^{-2}/year in summer. The autumn presents a linear decrease trend up to −0.75 kgm^{-2}/year.

This work will provide solid ancillary information for ongoing investigations on topics such as aerosol hygroscopic growth, forecast models, aerosol transport and ABLH calculations over this region by using MWR products.

Acknowledgments

This work was supported by the Andalusia Regional Government through project P12-RNM-2409; by the Spanish Ministry of Economy and Competitiveness through projects CGL2013-45410-R, CGL2015-73250-JIN and CGL2016-81092-R, the Excelence networkCGL2017-90884-REDT, the FPI grant (BES-2014- 068893), and the Juan de la Cierva grant IJCI-2016-30007; by the University of Granada through the Plan Propio Program P9 Call-2013 contract and the project UCE-PP2017. Andrés Bedoya has been supported by a grant for PhD studies in Colombia, COLCIENCIAS (Doctorado Nacional – 647), associated with the Physics Sciences program at the Universidad Nacional de Colombia, Sede Medellín and by the Asociación Universitaria Iberoamericana de Postgrado (AUIP). The study has also been supported by the Swiss National Science Foundation through project PZ00P2_168114. Financial support for EARLINET was through the ACTRIS Research Infrastructure Project EU H2020 (Grant agreement no. 654109), particularly through the TNA GRA-3 HYGROLIRA. The authors gratefully acknowledge the FEDER program for the instrumentation used in this work.

References

Alados-Arboledas, L., Müller, D., Guerrero-Rascado, J., Navas-Guzmán, F., Pérez-Ramírez, D., Olmo, F., 2011. Optical and microphysical properties of fresh biomass burning aerosol retrieved by Raman lidar, and star-and sun-photometry. Geophys. Res. Lett. 38, L01807. https://doi.org/10.1029/2010GL045999.

Bedoya-Velásquez, A.E., Navas-Guzmán, F., Granados-Muñoz, M.J., Titos, G., Román, R., Casquero-Vera, J.A., Ortiz-Amezcua, P., Benavent-Oltra, J.A., de Arruda Moreira, G., Montilla-Rosero, E., Hoyos, C.D., Artiñano, B., Coz, E., Olmo-Reyes, F.J., Alados-Arboledas, L., Guerrero-Rascado, J.L., 2018. Hygroscopic growth study in the framework of EARLINET during the SLOPE I campaign: synergy of remote sensing and in situ instrumentation. Atmos. Chem. Phys. 18, 7001–7017. https://doi.org/10.5194/acp-18-7001-2018.

Benavent-Oltra, J.A., Román, R., Granados-Muñoz, M.J., Pérez-Ramírez, D., Ortiz-Amezcua, P., Denjean, C., Lopatin, A., Lyamani, H., Torres, B., Guerrero-Rascado, J.L., Fuertes, D., Dubovik, O., Chaikovsky, A., Olmo, F.J., Mallet, M., Alados-Arboledas, L., 2017. Comparative assessment of GRASP algorithm for a dust event over Granada (Spain) during ChArMEx-ADRIMED 2013 campaign. Atmos. Meas. Tech. 10, 4439–4457. https://doi.org/10.5194/amt-10-4439-2017.

Bernet, L., Navas-Guzmán, F., Kampfer, N., 2017. The effect of cloud liquid water on tropospheric temperature retrievals from microwave measurements. Atmos. Meas. Tech. 10, 442–4437. https://doi.org/10.5194/amt-10-4421-2017.

Boucher, O., Randall, D., Artaxo, P., Bretherton, C., Feingold, G., Forster, P., Kerminen, V.-M., Kondo, Y., Liao, H., Lohmann, U., Rasch, P., Satheesh, S.K., Sherwood, S., Stevens, B., Zhang, X.Y., 2013. Clouds and Aerosols. In: Stocker, T.F., Qin, D., Plattner, G.-K., Tignor, M., Allen, S.K., Boschung, J., Nauels, A., Xia, Y., Bex, V., Midgley, P.M. (Eds.), Climate Change 2013: The Physical Science Basis. Contribution of Working Group I to the Fifth Assessment Report of the Intergovernmental Panel on Climate Change. Cambridge University Press, Cambridge, UK and New York, NY, USA.

Cazorla, A., Olmo, F.J., Alados-Arboledas, L., 2008. Development of a sky imager for cloud cover assessment. Opt. Soc. Am. A. 25 (1).

Cazorla, A., Husillos, C., Antón, M., Alados-Arboledas, L., 2015. Multi-exposure adaptive threshold technique for cloud detection with sky imagers. Sol. Energy 114, 268–277.

Cimini, D., Nelson, M., Güldner, J., Ware, R., 2015. Forecast indices from a ground-based microwave radiometer for operational meteorology. Atmos. Meas. Tech. 8, 315–333. https://doi.org/10.5194/amt-8-315-2015.

Coll, J., Aguilar, E., Ashcroft, L., 2017. Drought variability and change across the Iberian Peninsula. Theor. Appl. Climatol. 130, 901. https://doi.org/10.1007/s00704-016-1926-3.

Córdoba-Jabonero, C., Sorribas, M., Guerrero-Rascado, J.L., Adame, J.A., Hernández, Y., Lyamani, H., Cachorro, V., Gil, M., Alados-Arboledas, L., Cuevas, E., De La Morena, B., 2011. Synergetic monitoring of Saharan dust plumes and potential impact on surface: a case study of dust transport from Canary Islands to Iberian Peninsula. Atmos. Chem. Phys. 11 (7), 3067–3091.

Crewell, S., Löhnert, U., 2003. Accuracy of cloud liquid water path from ground-based microwave radiometry 2. Sensor accuracy and synergy. Radio Sci. 38, 8042. https://doi.org/10.1029/2002RS002634.

Crook, N.A., 1996. Sensitivity of moist convection forced by boundary layer processes to low-level thermodynamic fields. Mon. Weather Rev. 124, 1767–1785.

de Moreira, G.A., Guerrero-Rascado, J.L., Bravo-Aranda, J.A., Benavent-Oltra, J.A., Ortiz-Amezcua, P., Román, R., Bedoya-Velásquez, A.E., Landulfo, E., Alados-Arboledas, L., 2018. Study of the planetary boundary layer by microwave radiometer, elastic lidar and Doppler lidar estimations in Southern Iberian Peninsula. Atmos. Res. 213, 185–195. https://doi.org/10.1016/j.atmosres.2018.06.007.

Delanoe, J., Hogan, R.J., 2008. A variational scheme for retrieving ice cloud properties from combined radar, lidar, and infrared radiometer. J. Geophys. Res.-Atmos. 113. https://doi.org/10.1029/2007JD009000.

Granados-Muñoz, M.J., Navas-Guzmán, F., Bravo-Aranda, J.A., Guerrero-Rascado, J.L., Lyamani, H., Valenzuela, A., Titos, G., Fernández-Gálvez, J., Alados-Arboledas, L., 2015. Hygroscopic growth of atmospheric aerosol particles based on active remote sensing and radiosounding measurements: selected cases in southeastern Spain. Atmos. Meas. Tech. 8, 705–718.

Granados-Muñoz, M.J., Bravo-Aranda, J.A., Baumgardner, D., Guerrero-Rascado, J.L., Pérez-Ramírez, D., Navas-Guzmán, F., Veselovskii, I., Lyamani, H., Valenzuela, A., Olmo, F.J., Titos, G., Andrey, J., Chaikovsky, A., Dubovik, O., Gil-Ojeda, M., Alados-Arboledas, L., 2016. A comparative study of aerosol microphysical properties retrieved from ground-based remote sensing and aircraft in situ measurements during a Saharan dust event. Atmos. Meas. Tech. 9 (3), 1113–1133.

Guerrero-Rascado, J.L., Müller, D., Navas-Guzmán, F., Pérez-Ramirez, D., Alados-Arboledas, L., 2011. First results of aerosol microphysical properties by 3C2 raman lidar at Earlinet Granada station. Rom. J. Phys. 56, 467–475.

Guerrero-Rascado, J.L., Olmo, F.J., Avilés-Rodríguez, I., Navas-Guzmán, F., Pérez-Ramírez, D., Lyamani, H., Alados Arboledas, L., 2009. Extreme Saharan dust event over the southern Iberian Peninsula in september 2007: active and passive remote sensing from surface and satellite. Atmos. Chem. Phys. 9, 8453–8469. https://doi.org/10.5194/acp-9-8453-2009.

Guerrero-Rascado, J.L., Ruiz, B., Alados-Arboledas, L., 2008a. Multi-spectral Lidar characterization of the vertical structure of Saharan dust aerosol over southern Spain. Atmos. Environ. 42 (11) 2668–268.

Guerrero-Rascado, J.L., Ruiz, B., Chourdakis, G., Georgoussis, G., Alados-Arboledas, L., 2008b. One year of water vapour Raman lidar measurements at the Andalusian Centre for Environmental Studies (CEAMA). Int. J. Remote Sens. 29, 5437–5453.

Hoff, R.M., Hardesty, R.M., 2012. Thermodynamic profiling technologies workshop report to the National Science Foundation and the National Weather Service. NCAR Tech Note NCAR/TN-4881STR, 80 pp.

Holben, B.N., Eck, T.F., Slutsker, I., Tanre, D., Buis, J.P., Setzer, A., Vermote, E., Reagan, J.A., Kaufman, Y.J., Nakajima, T., Lavenus, F., Jankowiak, I., Smirnov, A., 1998. Aeronet –a federated instrument network and data archive for aerosol characterization. Remote Sens. Environ. 66, 1–16.

Holzworth, C.G., 1964. Estimates of mean maximum mixing depths in the contiguous United States. Mon. Weather Rev. 92, 235–242.

Kiehl, J., Trenberth, K.E., 1997. Earth's annual global mean energy budget. B. Am. Meteorol. Soc. 78, 197–208.

Löhnert, U., Crewell, S., 2003. Accuracy of cloud liquid water path from ground-based microwave radiometry 1. Dependency on cloud model statistics. Radio Sci. 38, 8041. https://doi.org/10.1029/2002RS002654.

Löhnert, U., Maier, O., 2012. Operational profiling of temperature using ground-based microwave radiometry at Payerne: prospects and challenges. Atmos. Meas. Tech. 5, 1121–1134. https://doi.org/10.5194/amt-5-1121-2012.

Löhnert, U., Crewell, S., Simmer, C., 2004. An integrated approach toward retrieving physically consistent profiles of temperature, humidity, and cloud liquid water. J. Appl. Meteorol. 43, 1295–1307.

Löhnert, U., Turner, D.D., Crewell, S., 2009. Ground-based temperature and humidity profiling using spectral infrared and microwave observations. Part I: simulated retrieval performance in clear-sky conditions. J. Appl. Meteorol. Climatol. 48, 1017–1032. https://doi.org/10.1175/2008JAMC2060.1.

Lyamani, H., Olmo, F.J., Alcántara, A., Alados-Arboledas, L., 2006a. Atmospheric aerosols during the 2003 heat wave in southeastern Spain I: spectral optical depth. Atmos. Environ. 40, 6453–6464.

Lyamani, H., Olmo, F.J., Alcántara, A., Alados-Arboledas, L., 2006b. Atmospheric aerosols during the 2003 heat wave in southeastern Spain II: microphysical columnar properties and radiative forcing. Atmos. Environ. 40, 6465–6476.

Lyamani, H., Olmo, F.J., Alados-Arboledas, L., 2010. Physical and optical properties of aerosols over an urban location in Spain: seasonal and diurnal variability. Atmos. Chem. Phys. 10, 239–254. https://doi.org/10.5194/acp-10-239-2010.

Lyamani, H., Fernández-Gálvez, J., Valenzuela, A., Antón, M., Alados, I., Titos, G., Olmo, F.J., 2012. Aerosol properties over two urban sites in South Spain during an extended stagnation episode in winter season. Atmos. Environ. 62, 424–432.

Maschwitz, G., Löhnert, U., Crewell, S., Rose, T., Turner, D.D., 2013. Investigation of ground based microwave radiometer calibration techniques at 530 hPa. Atmos. Meas. Tech. 6, 2641–2658. https://doi.org/10.5194/amt-6-2641-2013.

Mattis, I., Ansmann, A., Althausen, D., Jaenisch, V., Wandinger, U., Müller, D., Arshinov, Y.F., Bobrovnikov, S.M., Serikov, I.B., 2002. Relative-humidity profiling in the troposphere with a Raman lidar. Appl. Opt. 41, 6451–6462.

Navas-Guzmán, F., Bravo-Aranda, J.A., Guerrero-Rascado, J.L., Granados-Muñoz, M.J., Alados-Arboledas, L., 2013. Statistical analysis of aerosol optical properties retrieved by Raman lidar over Southeastern Spain. Tellus B 65, 21234.

Navas-Guzmán, F., Fernández-Gálvez, J., Granados-Muñoz, M.J., Guerrero-Rascado, J.L., Bravo-Aranda, J.A., Alados-Arboledas, L., 2014a. Tropospheric water vapour and relative humidiyty profiles from lidar and microwave radiometry. Atmos. Meas. Tech. 7, 1201–1211.

Navas-Guzmán, F., Stähli, O., Kämpfer, N., 2014b. An integrated approach toward the incorporation of clouds in the temperature retrievals from microwave measurements. Atmos. Meas. Tech. 7, 1619–1628. https://doi.org/10.5194/amt-7-1619-2014.

Navas-Guzmán, F., Kämpfer, N., Haefele, A., 2016. Validation of brightness and physical temperature from two scanning microwave radiometers in the 60 GHz O2 band using radiosonde measurements. Atmos. Meas. Tech. 9, 4587–4600.

Navas-Guzmán, F., Kämpfer, N., Schranz, F., Steinbrecht, W., Haefele, A., 2017. Intercomparison of stratospheric temperature profiles from a ground-based microwave radiometer with other techniques. Atmos. Chem. Phys. 17, 14085–14104. https://doi.org/10.5194/acp-17-14085-2017.

O'Connor, E.J., Illingworth, A.J., Brooks, I.M., Westbrook, C.D., Hogan, R.J., Davies, F., Brooks, B.J., 2010. A method for estimating the turbulent kinetic energy dissipation rate from a vertically-pointing Doppler lidar, and independent evaluation from balloon-borne in-situ measurements. J. Atmos. Ocean. Technol. 27 (10), 1652–1664.

Ortiz-Amezcua, P., Guerrero-Rascado, J.L., Granados-Muñoz, M.J., Bravo-Aranda, J.A., Alados-Arboledas, L., July 2013. Characterization of atmosferic aerosols for a long range transport of biomass burning particles from Canadian forest fires over the southern Iberian Peninsula in. ÓpticaPura y Aplicada 47, 43–49, 2014.

Ortiz-Amezcua, P., Guerrero-Rascado, J.L., Granados-Muñoz, M.J., Benavent-Oltra, J.A., Böckmann, C., Samaras, S., Stachlewska, I.S., Janicka, L., Baars, H., Bohlmann, S., Alados- Arboledas, L., 2017. Microphysical characterization of long-range transported biomass burning particles from North America at three EARLINET stations. Atmos. Chem. Phys. 17, 5931–5946. https://doi.org/10.5194/acp-17-5931-2017.

Río, S., Herrero, L., Pinto-Gomes, C., Penas, A., 2011. Spatial analysis of mean temperature trends in Spain over the period 1961–2006. Glob. Planet. Chang. 78 (1–2), 65–75. ISSN 0921–8181. https://doi.org/10.1016/j.gloplacha.2011.05.012.

Rodgers, C., 2000. Inverse Methods for Atmospheric Sounding: Theory and Practice. World Scientific Publishing Company, Incorporated, Singapore.

Román, R., Antón, M., Cazorla, A., Miguel, A.D., Olmo, F.J., Bilbao, J., Alados-Arboledas, L., 2012. Calibration of an all-sky camera for obtaining sky radiance at three wavelengths. Atmos. Meas. Tech. 5, 2013–2024. https://doi.org/10.5194/amt-5-2013-2012.

Román, R., Cazorla, A., Toledano, C., Olmo, F.J., Cachorro, V.E., de Frutos, A., Alados-Arboledas, L., 2017a. Cloud Cover Detection Combining High Dynamic Range Sky Images and Ceilometer Measurements. Atmospheric research. Vol. 196. pp. 224–236. https://doi.org/10.1016/j.atmosres.2017.06.006.

Román, R., Torres, B., Fuertes, D., Cachorro, V.E., Dubovik, O., Toledano, C., Cazorla, A., Barreto, A., Bosch, J.L., Lapyonok, T., González, R., Goloub, P., Perrone, M.P., Olmo, F.J., de Frutos, A., Alados-Arboledas, L., 2017b. Remote sensing of lunar aureole with

a sky camera: adding information in the nocturnal retrieval of aerosol properties with GRASP code. Remote Sens. Environ. 196, 238–252. https://doi.org/10.1016/j.rse.2017.05.013.

Rose, T., Crewell, S., Löhnert, U., Simmer, C., 2005. A network suitable microwave radiometer for operational monitoring of the cloudy atmosphere. Atmos. Res. 75 (3), 183–200.

Stankov, B.B., 1998. Multisensor retrieval of atmospheric properties. B. Am. Meteorol. Soc. 79 (2), 1835–1854. https://doi.org/10.1175/1520-0477(1998)079<1835:MROAP>2.0.CO.

Stevens, B., Bony, S., 2013. Water in the atmosphere. Phys. Today 66, 29. https://doi.org/10.1063/PT.3.2009.

Stull, R.B., 1988. An Introduction to Boundary Layer Meteorology. vol. 13 Kluwer Academic Publishers, the Netherlands, Dordrecht/Boston/London.

Stull, R.B., 2011. Meteorology for Scientists and Engineers, 3rd Edition. Uni. Of British Columbia.

Titos, G., Foyo-Moreno, I., Lyamani, H., Querol, X., Alastuey, A., Alados-Arboledas, L., 2012. Optical properties and chemical composition of aerosol particles at an urban location: an estimation of the aerosol mass scattering and absorption efficiencies. J. Geophys. Res. Atmos. 117, D04206. https://doi.org/10.1029/2011JD016671.

Titos, G., del Águila, A., Cazorla, A., Lyamani, H., Casquero-Vera, J.A., Colombi, C., Cuccia, E., Gianelle, V., Alastuey, A., Alasdos-Arboledas, L., 2017. Spatial and temporal variability of carbonaceous aerosols: assessing the impact of biomass burning in the urban environment. Sci. Total Environ. 578, 613–625. http://hdl.handle.net/10481/47096.

Turner, D.D., Clough, S.A., Liljegren, J.C., Clothiaux, E.E., Cady-Pereira, K.E., Gaustad, K.L., 2007. Retrieving liquid water path and precipitable water vapor from the atmospheric radiation measurement (ARM) microwave radiometers. IEEE Trans. Geosci. Remote Sens. 45, 3680–3690. https://doi.org/10.1109/TGRS.2007.903703.

Valenzuela, A., Olmo, F.J., Lyamani, H., Granados-Muñoz, M.J., Antón, M., Guerrero-Rascado, J.L., Quirantes, A., Toledano, C., Perez-Ramírez, D., Alados-Arboledas, L., 2014. Aerosol transport over the western mediterranean basin: evidence of the contribution of fine particles to desert dust plumes over Alborán island. J. Geophys. Res. 119 (24), 14,028–14,044.

Vaughan, G., Wareing, D., Thomas, L., Mitev, V., 1988. Humidity measurements in the free troposphere using Raman backscatter. Q. J. R. Meteorol. Soc. 114, 1471–1484.

Vogelmann, A.M., McFarquhar, G.M., Ogren, J.A., Turner, D.D., Comstock, J.M., Feingold, G., Long, C.N., Jonsson, H.H., Bucholtz, A., Collins, D.R., Diskin, G.S., Gerber, H., Lawson, R.P., Woods, R.K., Andrews, E., Yang, H., Chiu, J.C., Hartsock, D., Hubbe, J.M., Lo, C., Marshak, A., J, W., S, A.M., Toto, T., 2012. RACORO.: extended-term aircraft observations of boundary layer clouds. Bull. Am. Meteorol. Soc. 93, 861–878. https://doi.org/10.1175/BAMS-D-11-00189.1.